Experiments Division

ALBA Project Document No:	EDMS Document No.	Created: 6/9/2007	Pages: 19
EXD-BL22-XA-0001		Modified: 11/03/2009	Rev. No.: 4.0

Conceptual Design Report

*X-ray emission spectrometer
at the ALBA XAS beamline*

Prepared by:	Checked by:	Approved by:
Konstantin Klementiev	**Salvador Ferrer**	

Distribution List

Contents

Overview

This document describes the x-ray emission spectrometer to be installed at the ALBA XAS beamline. It features (i) large energy range 2–30 keV; (ii) energy resolution better than the natural widths of $K\alpha$ lines for elements S trough Ru; (iii) ample space for the insertion of large sample setups, up to Ø600 mm; (iv) energy dispersive images exempt from necessity of doing θ–2θ scans; the energy dispersion is possible in two scales: (a) over a single fluorescence line and (b) over several hundreds eV when several fluorescence lines are of interest; (v) compact design which allows for small vacuum tank that can be integrable into the common beamline vacuum system, so that the complete x-ray path source-optics-sample-crystal-detector be fully windowless; (vi) normal incidence to the sample, which (a) makes the usual side window in in-situ cells or sample vacuum volume not necessary, (b) has no depth related increase of the fluorescence source and (c) facilitates the polarization dependent studies (enables exact sample positioning relative to the polarization plane).

The spectrometer is based on the Rowland circle geometry with three exchangeable crystals Si(111), Si(220) and Ge(400) which have dynamical sagittal bending. The rectangular crystals are splitted into two halves and diced with facets of an optimum size of 2×2 mm^2.

1   Introduction

The modern x-ray emission spectrometers are mostly based on the so called Rowland circle geometry which allows for simultaneous focusing and energy discrimination. In this geometry the source (sample), the crystal analyzer and the detector lie on the Rowland circle and the crystal analyzer is bent, usually spherically, with the bending radius equal to the doubled radius of the Rowland circle. For better energy resolution and focusing the Bragg angle is attempted to be close to 90º. This has the following drawbacks:

- The sample-to-detector distance is small at $\theta \approx 90º$ (=$2R\sin 2\theta$, R being the Rowland circle radius). This makes impossible to use many required sample infrastructures: in-situ cells, cryostats, magnets, etc.

- Only a few fortunate combinations "a fluorescence line of an element" + "available crystals" result in $\theta \approx 90º$. For example, the maximum θ over all available silicon cuts (111) through (10,10,0) for $K\alpha_1$ lines of elements S through Nb is 89.35º (Ge $K\alpha_1$ with Si(555) or Si(751), see Table 1), but it is only 71.59º in average for these elements.

A usual positioning of the crystal analyzer is at 90º to the beam with the sample surface being at 45º to both the incident and emitted beams. This geometry has the following drawbacks:

- It requires an *ad hoc* side window in the sample vacuum volume and in-situ cells.

- The depth related increase of the fluorescence source size affects energy resolution. To avoid the source increase, one has to precisely install and tune small slits *near* the sample, which in turn affects the sample infrastructure.

- To measure polarization dependent spectra, the sample has to be frequently placed in normal incidence. To allow for outgoing fluorescence this positioning is never exactly normal.

The new design proposed in this Report eliminates all the aforementioned drawbacks. In the Report the following aspects are considered: scattering geometry, sagittal focusing, crystals shape, size and thickness, prerequisites for energy-dispersive configuration, possible asymmetrically cut crystals and energy resolution at different conditions.

The properties of the monochromatic beam assumed in this CDR are described in [1].

2 Angle range and scattering geometry

Let us restrict ourselves to the most usual crystals: silicon and germanium.

The upper Bragg angle is defined so that the sample-detector distance (see Figure 1) be >300 mm, plus some margin. For a usual Rowland circle radius of 0.5 m this results in θ_{max}=80°.

The cuts (111) and (220) are required at low energies. These crystal cuts together with their harmonics (green and magenta colors in Table 1) cover the energies 2–~22 keV if θ_{min}=48°. The exceptions are the very low energies (Cl and Ar) and the first few $3d$ elements: Ti, V, Cr and Mn. As the last ones are very important, a third crystal has to be considered. As seen in Table 1, the (400) cut is the best suitable (blue color). Whether Si or Ge crystals should be used will be considered in Section 9.
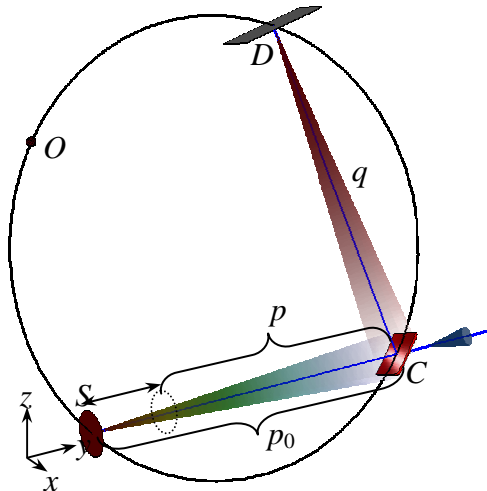
Figure 1. The scattering geometry. S = source (sample), C = crystal analyzer, D = detector, O = curvature center for C.

Sample-detector distance:
  $d_{SD}=2R\sin 2\theta$, (R = Rowland circle radius, here R=0.5 m)
Sample-crystal distance: $p_0=q=2R\sin\theta$,
Meridional crystal radius: $R_{mer}=2R$
Sagittal crystal radius:
  $R_{sag}=2\sin\theta\, pq/(p+q)$
  $R_{sag}(p=p_0)=2R\sin^2\theta$

	θ=35°	θ=45°	θ=80°
at $p=p_0$	R_{sag}=329 mm	R_{sag}=500 mm	R_{sag}=970 mm
at $p-p_0$=200 mm	R_{sag}=260 mm	R_{sag}=418 mm	R_{sag}=860 mm

To have an energy dispersive image rather than doing θ–2θ scan, the sample should go inside the Rowland circle (in fact, the complete setup should move to the static sample). This idea was proposed in [2], graphically described in (x, x', λ) coordinates in [3] and has recently been realized in an x-ray emission spectrometer [4].

To circumvent the problems related to the side position of the analyzer crystal (see Section 1), a back scattering at the sample is proposed. This requires the beam to pass through the crystal analyzer. For this, a pinhole or a gap is needed. The gap between the two halves of the crystal must lie in the diffraction plane because when the sample is inside the Rowland circle different parts of the crystal work for different energies; thus a gap perpendicular to the diffraction plane would lead to a corresponding gap in the measured spectrum. Moreover, the gap in the diffraction plane would make the θ–2θ alignment easier. The last argument also favors to a gap rather than to a pinhole.

The diffraction plane is considered to be vertical because the beam size is smaller vertically than horizontally [1]. See also Section 14 for further considerations.

Table 1. Bragg angles for $K\alpha_1$, $K\beta_1$ and K-edges for Si and Ge crystals.

$K\alpha 1$

No.	Elem.	d (Å)	Si (111)	Si (220)	Si (311)	Si (400)	Si (331)	Si (422)	Si (333,511)	Si (440)	Si (444)	Si (660)	Si (555,751)	Si (880)	Si (777)	Si (888)	Si (10,10,0)	Ge (111)	Ge (220)	Ge (311)	Ge (400)	Ge (331)	Ge (422)	Ge (333,511)	Ge (440)	Ge (444)	Ge (660)	Ge (555,751)	Ge (880)	Ge (777)	Ge (888)	Ge (10,10,0)
			3.1354	1.9200	1.6374	1.3577	1.2459	1.1085	1.0451	0.9600	0.7839	0.6400	0.6271	0.4800	0.4479	0.3919	0.3840	3.2663	2.0002	1.7058	1.4143	1.2979	1.1548	1.0888	1.0001	0.8166	0.6667	0.6533	0.5000	0.4666	0.4083	0.4000
16	S	2307.84	58.95															55.32														
17	Cl	2622.39	48.93															46.36														
18	Ar	2957.7	41.95															39.92														
19	K	3313.8	36.63	76.99														34.94	69.27													
20	Ca	3691.68	32.38	61.00														30.94	57.09	79.88											
21	Sc	4090.6	28.90	52.12	67.75													27.64	49.26	62.68											
22	Ti	4510.84	26.00	45.71	57.07													24.88	43.40	53.68	76.33										
23	V	4952.2	23.53	40.69	49.86	67.22												22.54	38.74	47.21	62.26	74.69									
24	Cr	5414.72	21.42	36.60	44.36	57.49	66.77											20.52	34.92	42.16	54.05	61.90	82.48								
25	Mn	5898.75	19.58	33.19	39.93	50.72	57.51	71.45										18.77	31.70	38.03	47.99	54.07	65.51	74.85							
26	Fe	6403.84	17.98	30.28	36.24	45.48	50.99	60.84	67.86									17.24	28.95	34.58	43.19	48.23	56.96	62.76	75.46						
27	Co	6930.32	16.58	27.77	33.11	41.21	45.89	53.80	58.86	68.71								15.89	26.57	31.63	39.23	43.57	50.77	55.24	63.43						
28	Ni	7478.15	15.33	25.58	30.42	37.63	41.71	48.40	52.48	59.71								14.70	24.48	29.08	35.88	39.70	45.88	49.59	55.99						
29	Cu	8047.78	14.22	23.65	28.06	34.57	38.19	44.02	47.48	53.36	79.33							13.64	22.65	26.85	33.00	36.41	41.84	45.03	50.37	70.62					
30	Zn	8638.86	13.23	21.95	25.99	31.91	35.17	40.34	43.36	48.37	66.27							12.69	21.02	24.88	30.49	33.57	38.42	41.23	45.85	61.50					
31	Ga	9251.74	12.34	20.43	24.16	29.57	32.54	37.19	39.88	44.26	58.74							11.84	19.57	23.13	28.28	31.08	35.47	37.98	42.07	55.14					
32	Ge	9886.42	11.54	19.06	22.52	27.51	30.22	34.45	36.87	40.78	53.13	78.45	89.35					11.07	18.27	21.57	26.32	28.89	32.89	35.16	38.83	50.17	70.13	73.71			
33	As	10543.7	10.81	17.83	21.04	25.66	28.16	32.03	34.23	37.77	48.60	66.73	69.65					10.37	17.09	20.16	24.56	26.94	30.61	32.69	36.01	46.06	61.87	64.16			
34	Se	11222.4	10.15	16.72	19.72	24.01	26.32	29.89	31.91	35.13	44.81	59.67	61.75					9.74	16.03	18.90	22.99	25.19	28.58	30.49	33.53	42.57	55.95	57.74			
35	Br	11924.2	9.54	15.71	18.51	22.51	24.66	27.97	29.83	32.79	41.55	54.32	56.00					9.16	15.07	17.75	21.57	23.61	26.76	28.52	31.32	39.54	51.24	52.73			
36	Kr	12649	8.99	14.79	17.42	21.16	23.16	26.24	27.96	30.70	38.70	49.97	51.40					8.63	14.18	16.70	20.27	22.19	25.11	26.75	29.34	36.88	47.31	48.61	78.55		
37	Rb	13395.3	8.49	13.95	16.42	19.93	21.81	24.68	26.28	28.82	36.19	46.31	47.56	74.61				8.15	13.38	15.74	19.10	20.89	23.63	25.15	27.56	34.52	43.96	45.11	67.74	82.66	
38	Sr	14165	8.02	13.18	15.50	18.80	20.56	23.25	24.76	27.12	33.94	43.14	44.26	65.75	77.70			7.70	12.64	14.87	18.03	19.71	22.27	23.70	25.95	32.41	41.03	42.06	61.07	69.70	
39	Y	14958.4	7.60	12.47	14.66	17.77	19.43	21.95	23.36	25.57	31.92	40.36	41.37	59.70	67.70			7.29	11.96	14.06	17.04	18.62	21.03	22.37	24.48	30.50	38.43	39.38	55.97	62.64	
40	Zr	15775.1	7.20	11.81	13.89	16.82	18.39	20.76	22.09	24.16	30.09	37.88	38.80	54.95	61.32			6.91	11.33	13.32	16.13	17.62	19.89	21.16	23.14	28.77	36.12	36.98	51.80	57.37	74.26	79.22
41	Nb	16615.1	6.83	11.21	13.17	15.95	17.43	19.67	20.92	22.87	28.42	35.66	36.51	51.01	56.41	72.17	76.32	6.56	10.75	12.63	15.30	16.71	18.85	20.04	21.91	27.19	34.03	34.83	48.26	53.09	66.04	68.86
42	Mo	17479.3	6.49	10.64	12.51	15.14	16.54	18.66	19.84	21.68	26.90	33.65	34.44	47.63	52.35	64.81	67.45	6.23	10.21	12.00	14.52	15.86	17.89	19.01	20.77	25.74	32.14	32.88	45.17	49.47	60.30	62.45
43	Tc	18367.1	6.18	10.12	11.90	14.39	15.72	17.73	18.84	20.58	25.50	31.83	32.56	44.68	48.90	59.45	61.51	5.93	9.71	11.41	13.81	15.07	16.99	18.06	19.72	24.41	30.41	31.11	42.45	46.33	55.76	57.53
44	Ru	19279.2	5.89	9.64	11.33	13.70	14.96	16.86	17.92	19.57	24.22	30.16	30.85	42.06	45.88	55.13	56.86	5.65	9.25	10.87	13.14	14.36	16.17	17.18	18.75	23.19	28.83	29.49	40.02	43.56	51.96	53.49
45	Rh	20216.1	5.61	9.19	10.79	13.05	14.25	16.06	17.06	18.63	23.03	28.63	29.28	39.70	43.20	51.48	52.99	5.39	8.82	10.36	12.52	13.67	15.40	16.36	17.86	22.06	27.38	28.00	37.82	41.09	48.68	50.05
46	Pd	21177.1	5.36	8.77	10.30	12.45	13.59	15.31	16.27	17.75	21.94	27.22	27.83	37.58	40.81	48.32	49.67	5.14	8.42	9.88	11.95	13.03	14.68	15.60	17.02	21.01	26.04	26.62	35.83	38.86	45.81	47.03
47	Ag	22162.9	5.12	8.38	9.84	11.89	12.97	14.62	15.52	16.94	20.91	25.92	26.49	35.64	38.64	45.54	46.75	4.91	8.04	9.44	11.41	12.45	14.02	14.89	16.24	20.03	24.80	25.35	34.01	36.83	43.24	44.36
48	Cd	23173.6	4.89	8.01	9.40	11.36	12.40	13.96	14.83	16.18	19.95	24.71	25.25	33.87	36.67	43.04	44.16	4.70	7.69	9.02	10.90	11.89	13.39	14.22	15.51	19.12	23.66	24.17	32.34	34.98	40.94	41.97
49	In	24209.7	4.68	7.66	9.00	10.87	11.86	13.36	14.18	15.47	19.07	23.58	24.10	32.24	34.87	40.79	41.82	4.50	7.36	8.63	10.43	11.38	12.81	13.60	14.84	18.28	22.59	23.08	30.80	33.28	38.84	39.80

$K\beta 1$

No.	Elem.	d (Å)	Si (111)	Si (220)	Si (311)	Si (400)	Si (331)	Si (422)	Si (333,511)	Si (440)	Si (444)	Si (660)	Si (555,751)	Si (880)	Si (777)	Si (888)	Si (10,10,0)	Ge (111)	Ge (220)	Ge (311)	Ge (400)	Ge (331)	Ge (422)	Ge (333,511)	Ge (440)	Ge (444)	Ge (660)	Ge (555,751)	Ge (880)	Ge (777)	Ge (888)	Ge (10,10,0)
			3.1354	1.9200	1.6374	1.3577	1.2459	1.1085	1.0451	0.9600	0.7839	0.6400	0.6271	0.4800	0.4479	0.3919	0.3840	3.2663	2.0002	1.7058	1.4143	1.2979	1.1548	1.0888	1.0001	0.8166	0.6667	0.6533	0.5000	0.4666	0.4083	0.4000
16	S	2464.04	53.36															50.38														
17	Cl	2815.6	44.60															42.38														
18	Ar	3190.5	38.29															36.50	76.27													
19	K	3589.6	33.42	64.09														31.92	59.70													
20	Ca	4012.7	29.52	53.57	70.65													28.23	50.57	64.92												
21	Sc	4460.5	26.31	46.37	58.08													25.18	44.01	54.56	79.31										
22	Ti	4931.81	23.63	40.89	50.14	67.79												22.63	38.93	47.47	62.72	75.58									
23	V	5427.29	21.36	36.51	44.23	57.28	66.46											20.47	34.82	42.04	53.86	61.65	81.54								
24	Cr	5946.71	19.42	32.88	39.54	50.16	56.80	70.12	85.90									18.61	31.41	37.67	47.48	53.44	64.52	73.23							
25	Mn	6490.45	17.74	29.83	35.68	44.71	50.05	59.50	66.05	84.21								17.00	28.52	34.05	42.48	47.38	55.80	61.31	72.75						
26	Fe	7057.98	16.27	27.22	32.44	40.31	44.83	52.40	57.18	66.19								15.60	26.05	30.99	38.39	42.59	49.52	53.78	61.43						
27	Co	7649.43	14.98	24.97	29.67	36.65	40.58	46.98	50.84	57.58								14.37	23.90	28.37	34.96	38.64	44.57	48.10	54.13	82.96					
28	Ni	8264.66	13.84	23.00	27.26	33.54	37.02	42.58	45.86	51.38	73.12							13.28	22.02	26.09	32.03	35.31	40.51	43.55	48.59	66.72					
29	Cu	8905.29	12.83	21.26	25.16	30.85	33.97	38.90	41.76	46.48	62.63							12.31	20.37	24.09	29.48	32.44	37.07	39.75	44.11	58.48					
30	Zn	9572	11.92	19.71	23.30	28.49	31.32	35.75	38.29	42.42	55.71							11.44	18.89	22.31	27.25	29.93	34.11	36.49	40.36	52.48	76.26	82.48			
31	Ga	10264.2	11.11	18.33	21.64	26.41	29.00	33.01	35.30	38.98	50.40	70.68	74.39					10.66	17.58	20.74	25.28	27.73	31.53	33.69	37.15	47.70	64.94	67.60			
32	Ge	10982.1	10.37	17.10	20.17	24.57	26.93	30.61	32.69	36.01	46.17	61.88	64.18					9.95	16.39	19.33	23.52	25.78	29.21	31.23	34.36	43.73	57.85	59.78			
33	As	11726.2	9.71	15.98	18.84	22.92	25.11	28.48	30.39	33.41	42.41	55.69	57.46					9.31	15.33	18.05	21.95	24.04	27.24	29.05	31.91	40.35	52.46	54.03			
34	Se	12495.9	9.10	14.97	17.64	21.43	23.47	26.59	28.34	31.32	39.26	50.82	52.29					8.74	14.36	16.91	20.53	22.47	25.43	27.14	29.74	37.41	48.08	49.41	82.80		
35	Br	13291.4	8.55	14.06	16.55	20.09	21.98	24.88	26.50	29.07	36.51	46.78	48.05	76.33				8.21	13.48	15.87	19.25	21.06	23.82	25.37	27.80	34.83	44.39	45.56	68.86	88.31	
36	Kr	14112	8.05	13.23	15.56	18.88	20.65	23.35	24.85	27.23	34.08	43.34	44.47	66.23	78.73			7.73	12.69	14.92	18.10	19.78	22.36	23.80	26.06	32.55	41.21	42.26	61.46	70.30	
37	Rb	14961.3	7.59	12.46	14.66	17.77	19.43	21.95	23.36	25.57	31.91	40.35	41.36	59.68	67.68			7.29	11.96	14.06	17.04	18.62	21.03	22.37	24.48	30.49	38.42	39.37	55.96	62.62	
38	Sr	15835.7	7.17	11.76	13.83	16.76	18.31	20.68	22.00	24.07	29.96	37.71	38.63	54.64	60.92	87.23		6.88	11.29	13.27	16.07	17.56	19.82	21.07	23.04	28.65	35.96	36.82	51.52	57.03	73.50	78.12
39	Y	16737.8	6.78	11.12	13.07	15.83	17.29	19.52	20.76	22.69	28.20	35.36	36.20	50.50	55.78	70.91	74.69	6.51	10.67	12.54	15.18	16.58	18.71	19.89	21.74	26.97	33.75	34.54	47.79	52.54	65.11	67.80
40	Zr	17667.8	6.43	10.53	12.37	14.98	16.36	18.45	19.62	21.44	26.59	33.25	34.02	46.97	51.57	63.54	66.02	6.17	10.10	11.87	14.36	15.68	17.69	18.80	20.54	25.45	31.75	32.49	44.56	48.76	59.25	61.30
41	Nb	18622.5	6.09	9.98	11.73	14.19	15.50	17.48	18.57	20.29	25.13	31.34	32.06	43.91	48.00	58.14	60.10	5.85	9.58	11.25	13.61	14.86	16.75	17.80	19.44	24.06	29.95	30.64	41.74	45.54	54.62	56.32
42	Mo	19608.3	5.79	9.48	11.13	13.47	14.70	16.57	17.61	19.23	23.79	29.60	30.28	41.20	44.90	53.77	55.42	5.55	9.09	10.68	12.92	14.10	15.89	16.88	18.43	22.78	28.31	28.94	39.22	42.65	50.75	52.21
43	Tc	20619	5.50	9.01	10.58	12.79	13.96	15.74	16.72	18.25	22.55	28.02	28.65	38.78	42.16	50.10	51.53	5.28	8.65	10.15	12.27	13.39	15.09	16.03	17.50	21.60	26.80	27.40	36.96	40.12	47.44	48.73
44	Ru	21656.8	5.24	8.57	10.07	12.17	13.28	14.96	15.90	17.35	21.42	26.57	27.16	36.61	39.72	46.92	48.20	5.03	8.23	9.66	11.68	12.74	14.35	15.24	16.63	20.52	25.43	25.99	34.92	37.84	44.52	45.69
45	Rh	22723.6	4.99	8.17	9.59	11.59	12.65	14.25	15.13	16.51	20.37	25.23	25.79	34.63	37.52	44.11	45.27	4.79	7.84	9.20	11.12	12.13	13.66	14.51	15.83	19.52	24.15	24.68	33.06	35.78	41.93	43.00
46	Pd	23818.7	4.76	7.79	9.15	11.05	12.06	13.58	14.42	15.73	19.39	24.00	24.52	32.83	35.53	41.61	42.67	4.57	7.48	8.78	10.60	11.57	13.03	13.83	15.08	18.59	22.98	23.48	31.36	33.90	39.60	40.59
47	Ag	24942.4	4.55	7.44	8.73	10.55	11.51	12.96	13.76	15.00	18.49	22.85	23.35	31.18	33.70	39.36	40.33	4.36	7.14	8.38	10.12	11.04	12.43	13.20	14.39	17.72	21.89	22.36	29.80	32.18	37.50	38.43
48	Cd	26095.5	4.35	7.11	8.34	10.08	10.99	12.37	13.14	14.33	17.64	21.79	22.26	29.66	32.03	37.31	38.22	4.17	6.82	8.01	9.67	10.55	11.87	12.60	13.74	16.91	20.87	21.32	28.36	30.60	35.58	36.43
49	In	27275.9	4.16	6.80	7.98	9.64	10.51	11.83	12.56	13.69	16.85	20.80	21.25	28.26	30.49	35.44	36.29	3.99	6.52	7.66	9.25	10.09	11.35	12.05	13.14	16.16	19.93	20.36	27.03	29.15	33.83	34.62

K-edge

No.	Elem.	d (Å)	Si (111)	Si (220)	Si (311)	Si (400)	Si (331)	Si (422)	Si (333,511)	Si (440)	Si (444)	Si (660)	Si (555,751)	Si (880)	Si (777)	Si (888)	Si (10,10,0)	Ge (111)	Ge (220)	Ge (311)	Ge (400)	Ge (331)	Ge (422)	Ge (333,511)	Ge (440)	Ge (444)	Ge (660)	Ge (555,751)	Ge (880)	Ge (777)	Ge (888)	Ge (10,10,0)
			3.1354	1.9200	1.6374	1.3577	1.2459	1.1085	1.0451	0.9600	0.7839	0.6400	0.6271	0.4800	0.4479	0.3919	0.3840	3.2663	2.0002	1.7058	1.4143	1.2979	1.1548	1.0888	1.0001	0.8166	0.6667	0.6533	0.5000	0.4666	0.4083	0.4000
16	S	2472	53.11															50.15														
17	Cl	2822.4	44.47															42.26														
18	Ar	3205.9	38.08															36.30	75.19													
19	K	3608.4	33.23	63.48														31.73	59.20													
20	Ca	4038.5	29.31	53.08	69.63													28.03	50.13	64.15												
21	Sc	4492	26.11	45.95	57.44													24.99	43.63	54.00	77.36										
22	Ti	4966	23.46	40.55	49.67	66.85												22.47	38.62	47.04	61.96	74.12									
23	V	5465	21.21	36.21	43.85	56.67	65.57											20.32	34.55	41.68	53.82	60.93	79.20								
24	Cr	5989	19.28	32.62	39.21	49.68	56.18	69.03	82.05									18.48	31.16	37.36	47.04	52.89	63.68	71.94							
25	Mn	6539	17.60	29.59	35.38	44.29	49.55	58.78	65.11	80.94								16.87	28.29	33.76	42.09	46.95	55.28	60.55	71.43						
26	Fe	7112	16.14	27.00	32.16	39.94	44.40	51.84	56.51	65.22								15.48	25.84	30.73	38.05	42.19	49.01	53.19	60.64						
27	Co	7709	14.86	24.76	29.41	36.32	40.20	46.50	50.30	56.89								14.25	23.71	28.13	34.65	38.29	44.14	47.61	53.52	80.00					
28	Ni	8333	13.73	22.80	27.02	33.23	36.66	42.15	45.38	50.80	71.64							13.17	21.83	25.86	31.74	34.97	40.11	43.10	48.06	65.65					
29	Cu	8979	12.72	21.07	24.94	30.57	33.65	38.52	41.35	45.99	61.74							12.20	20.19	23.88	29.22	32.14	36.79	39.36	43.66	57.73					
30	Zn	9659	11.81	19.53	23.08	28.21	31.01	35.38	37.89	41.95	54.96							11.33	18.72	22.10	26.99	29.64	33.76	36.12	39.92	51.81	74.29	79.26			
31	Ga	10367	10.99	18.15	21.42	26.13	28.68	32.64	34.90	38.53	49.72	69.12	72.47					10.55	17.40	20.52	25.01	27.43	31.19	33.31	36.72	47.08	63.75	66.26			
32	Ge	11103	10.26	16.91	19.94	24.28	26.62	30.24	32.29	35.56	45.82	60.54	62.92					9.84	16.21	19.11	23.25	25.48	28.91	30.85	33.94	43.14	56.87	58.73			
33	As	11867	9.59	15.79	18.60	22.63	24.79	28.12	29.99	32.97	41.79	54.71	56.41					9.20	15.14	17.83	21.68	23.73	26.90	28.67	31.49	39.77	51.58	53.10			
34	Se	12658	8.99	14.78	17.40	21.14	23.15	26.22	27.94	30.67	38.67	49.93	51.35					8.62	14.17	16.69	20.26	22.17	25.09	26.72	29.32	36.85	47.27	48.56	78.35		
35	Br	13474	8.44	13.86	16.32	19.81	21.67	24.52	26.12	28.64	35.94	45.96	47.20	73.43				8.10	13.30	15.65	18.98	20.76	23.48	25.00	27.39	34.29	43.64	44.77	66.94	80.41	
36	Kr	14326	7.93	13.02	15.32	18.59	20.32	22.98	24.46	26.79	33.51	42.63	43.63	64.35	75.03			7.61	12.49	14.70	17.82	19.48	22.01	23.42	25.64	32.00	40.47	41.48	59.93	68.03	
37	Rb	15200	7.47	12.26	14.42	17.48	19.11	21.59	22.97	25.11	31.35	39.59	40.57	58.17	65.58			7.17	11.77	13.83	16.76	18.31	20.68	22.00	24.07	29.96	37.71	38.63	54.65	60.93	87.34
38	Sr	16105	7.05	11.56	13.60	16.47	18.00	20.37	21.65	23.65	29.55	37.05	37.94	53.50	59.15	79.15		6.77	11.10	13.04	15.79	17.24	19.47	20.70	22.63	28.12	35.26	36.10	50.33	55.58	70.52	74.20
39	Y	17038	6.66	10.92	12.84	15.54	16.98	19.16	20.37	22.27	27.66	34.65	35.47	49.29	54.32	68.18	71.35	6.40	10.48	12.32	14.91	16.28	18.37	19.52	21.33	26.46	33.07	33.80	46.69	51.24	63.02	65.44
40	Zr	17998	6.31	10.33	12.14	14.70	16.05	18.10	19.24	21.03	26.07	32.56	33.32	45.85	50.26	61.50	63.76	6.05	9.92	11.65	14.10	15.39	17.35	18.44	20.15	24.95	31.11	31.83	43.34	47.58	57.52	59.43
41	Nb	18986	5.98	9.79	11.50	13.92	15.19	17.13	18.20	19.88	24.62	30.68	31.38	42.86	46.80	56.42	58.24	5.74	9.40	11.04	13.35	14.57	16.42	17.45	19.06	23.57	29.32	29.99	40.77	44.41	53.10	54.71
42	Mo	20000	5.68	9.29	10.91	13.20	14.41	16.24	17.25	18.84	23.29	28.97	29.62	40.22	43.79	52.27	53.82	5.45	8.91	10.47	12.66	13.82	15.57	16.54	18.06	22.31	27.70	28.33	38.31	41.63	49.39	50.79
43	Tc	21044	5.39	8.83	10.36	12.53	13.68	15.41	16.37	17.87	22.04	27.38	27.99	37.86	41.17	48.73	50.10	5.17	8.47	9.94	12.01	13.12	14.78	15.70	17.13	21.15	26.22	26.80	36.09	39.15	46.18	47.43
44	Ru	22117	5.13	8.39	9.86	11.91	13.00	14.65	15.56	16.98	20.95	25.97	26.55	35.73	38.74	45.66	46.88	4.92	8.06	9.46	11.43	12.47	14.05	14.92	16.28	20.08	24.86	25.41	34.09	36.92	43.35	44.48
45	Rh	23220	4.88	7.99	9.38	11.34	12.37	13.94	14.81	16.16	19.91	24.65	25.20	33.85	36.63	43.02	44.16	4.69	7.67	9.00	10.88	11.87	13.37	14.19	15.48	19.08	23.61	24.12	32.30	34.96	41.03	42.04
46	Pd	24350	4.66	7.62	8.94	10.81	11.79	13.28	14.10	15.38	18.95	23.44	23.95	32.03	34.64	40.51	41.53	4.47	7.31	8.58	10.37	11.31	12.74	13.52	14.75	18.17	22.45	22.94	30.61	33.07	38.58	39.52
47	Ag	25514	4.45	7.27	8.53	10.31	11.25	12.66	13.44	14.66	18.05	22.32	22.80	30.39	32.85	38.31	39.25	4.27	6.98	8.19	9.89	10.79	12.15	12.90	14.06	17.31	21.37	21.84	29.15	31.38	36.52	37.40
48	Cd	26711	4.24	6.94	8.15	9.84	10.74	12.08	12.83	13.99	17.22	21.26	21.72	28.91	31.21	36.31	37.18	4.07	6.66	7.82	9.44	10.30	11.59	12.31	13.42	16.51	20.37	20.81	27.65	29.83	34.64	35.46
49	In	27940	4.06	6.64	7.79	9.41	10.26	11.55	12.26	13.36	16.44	20.28	20.72	27.53	29.69	34.48	35.30	3.90	6.37	7.47	9.03	9.84	11.08	11.76	12.82	15.77	19.44	19.86	26.34	28.39	32.92	33.69

3   Notes on ray tracing

All further conclusions are based upon ray tracing done with ED-Shadowrunner [5] which is a Matlab script running the Shadow ray tracing code [6,7] and visualizing the energy-, intensity- and position- distributions of sampling rays.

Unless otherwise specified, the beam size at the sample was taken to be 300h×200v μm^2, which follows from a conservative estimation for the slope error of the collimating mirror and for the heat load on the 1st monochromator crystal [1].

Unless otherwise specified, the analyzer crystal is Si(444).

All images were taken at the detector position normal to the crystal-detector direction.

The radius of the Rowland circle was taken equal to 0.5 m.

NB: For better readability of this document the ray-traced images were strongly reduced in size. You can better view these images on screen with a high magnification (>500%).

4   Sagittal focusing

Table 2. Images for a fixed (optimized at 55º) and variable sagittal bending radii at different Bragg angles.
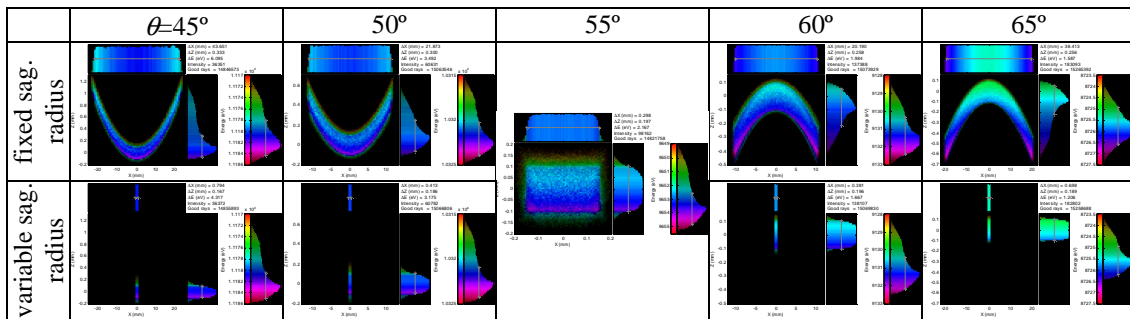
Table 3. Images for a fixed (optimized for on-circle geometry) and variable sagittal bending radii at different in-circle coordinates.
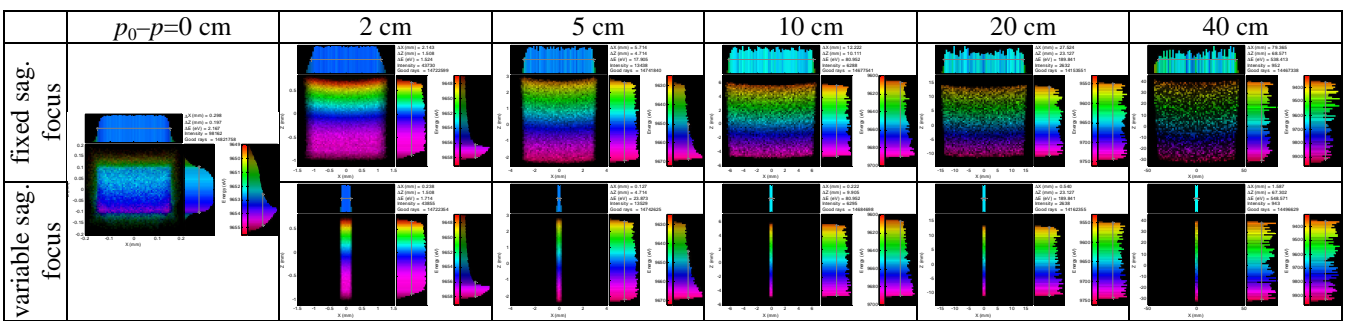
Observations:

A fixed sagittal radius results in an increase of the horizontal (sagittal) image size when doing θ scan or moving the sample into the Rowland circle. Here the sagittal focusing was optimized for θ=55º and the on-circle sample position. The variation $\Delta\theta$=±10º increases the image width by ~40 mm, and in going into the Rowland circle by 400 mm the image width increases by ~80 mm.

The energy distribution is not noticeably affected by sagittal focusing.

Summary:

Dynamic sagittal bending is required as a function of Bragg angle and in-circle coordinate. Otherwise the detector size has to be large and for energy dispersive images a 2D detector will be demanded instead of a 1D detector that suffices for the sagittally focused images.

The dynamic sagittal focusing is implied in all following ray tracing exercises.

5 Crystal shape

Table 4. Energy dispersive images for a round (Ø100 mm) and a square crystal (89 mm)^2 of the same area. The relative flux is given above each image for an energy-uniform (in ph/s/eV) isotropic source (transmittivity $T = (I/N_{rays}){\cdot}(\Delta E_{geom.source}/\Delta E){\cdot}(\Omega_{geom.source}/\Omega)$, flux $\Phi \propto T{\cdot}\Omega{\cdot}\Delta E$, where the subscript 'geom.source' refers to the ray tracing source, ΔE and Ω are energy- and angle acceptance of the crystal.

	p_0–p=0 cm	2 cm	5 cm	10 cm	20 cm	40 cm
round	≡100%	90%	117%	132%	184%	381%
square	102%	89%	117%	132%	180%	384%
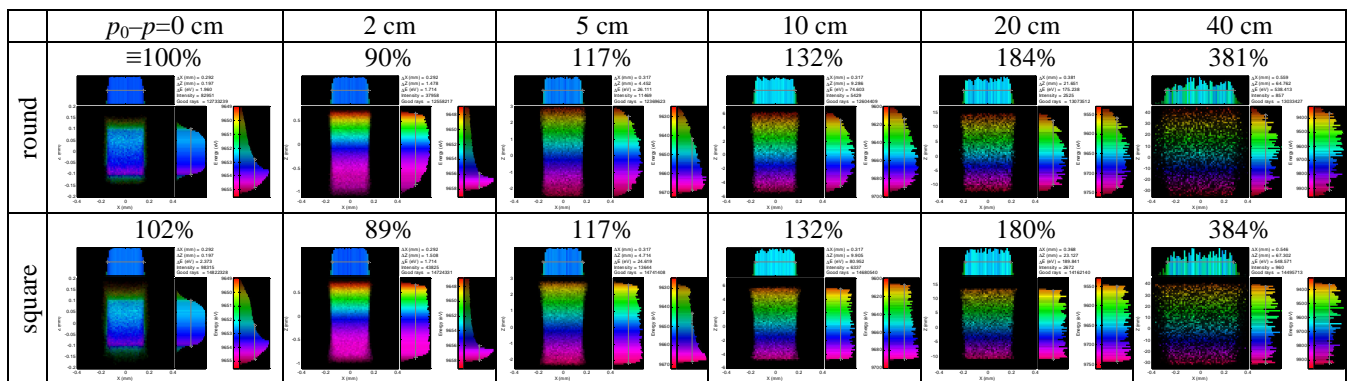
Observations:

The *z*-distributions for the round (square) crystal are non-linear (linear).

Summary:

The rectangular shape allows for an easy linear correction for the intensity of the fluorescence lines along the energy dispersive *z*-coordinate.

The rectangular shape allows for simple rectangular slits which must be, however, inclined parallel to the crystal.

The square shape is implied in all following ray tracing exercises.

6 Diced crystal
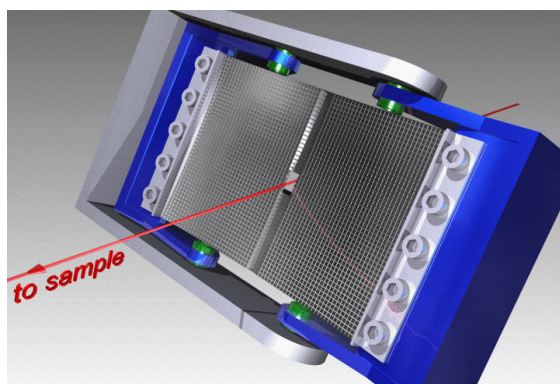
Figure 2. A diced analyzer crystal with sagittal bender and fixed meridional radius (see animation on: www.cells.es/Beamlines/XAS/).

Diced crystals allow for energy dispersive images within a single fluorescence line. Thus there will be two levels of energy dispersion:

1) in the range of some eV for a single fluorescence line, where the line profile is measured without θ–2θ scan;

2) in the range of up to several hundreds eV for several fluorescence lines, where the fluorescence spectrum is measured without θ–2θ scan;

Implementations of diced crystals have been published elsewhere (Ref. [8] and Refs. therein).

Table 5. Energy dispersive images for not-diced and diced crystals with different square facet sizes. The Bragg angle θ=55°. Above the images, the flux is given for a uniform (in ph/s/bw) fluorescence source (i.e. when each characteristic line has equal total number of photons, see Section 10 for details), relative to the Si(111) not-diced case along with the flat top width in the energy distribution (in the relevant cases). The image sizes are the same for the same facet size.

	$\Delta E K\alpha$ (eV)	not-diced	1 mm	1.5 mm	2 mm	2.5 mm	3 mm
Si111	0.65	≡100%	66%	1 eV 54%	2 eV 43%	2.7 eV 35%	3.5 eV 31%
Ge111		167%	127%	104%	1 eV 92%	2 eV 77%	3 eV 68%
Si220	1.05	92%	2 eV 52%	2 eV 39%	3 eV 33%	5 eV 26%	6 eV 24%
Ge220		178%	119%	1 eV 92%	3 eV 77%	4 eV 63%	5 eV 56%
Si400	1.35	45%	24%	2 eV 19%	5 eV 16%	6 eV 13%	9 eV 11%
Ge400		103%	59%	2.5 eV 45%	4 eV 37%	6.5 eV 30%	8 eV 26%
Si444	2.8	11%	6%	4 eV 4%	8 eV 4%	12 eV 3%	15 eV 3%
Ge444		24%	13%	5 eV 10%	7 eV 8%	10 eV 7%	15 eV 6%
Si888	7.3	1.1%	0.6%	0.5%	?? eV 0.4%	?? eV 0.3%	?? eV 0.3%
Ge888		2.6%	1.3%	1.0%	20 eV 0.8%	25 eV 0.7%	35 eV 0.6%

Observations:

The Ge crystals give ~2 times higher flux than the Si crystals.

For the same crystal type the flux decreases for larger facets.

The image size is the doubled facet size plus the source size, in z-coordinate it is then reduced by $\sin\theta$.

At small facet sizes the energy distributions are peak-like, at large facet sizes the energy distributions have flat top.

Summary:

In terms of flux Ge crystals are preferable to Si ones if energy resolution is acceptable.

A flat top in energy distribution assumes that an analyzed fluorescence line will not be distorted within this flat energy region. Because a Lorentzian line has long tails, to fully contain the line within the flat top is impossible. The target flat width was set here equal to the triple FWHM of the line. This target is met *for all the crystals* at the facet size **2 mm** (cf. the flat top width with the approximate line width given in the 2nd column in Table 5). A further increase of the facet size would decrease the efficiency: Only a part of each crystal facet would work for the fluorescence line, the remaining area being just spectator.

The crystals in diced form with 2 mm facets are implied in all following ray tracing exercises.

7   Symmetric vs. asymmetric crystal
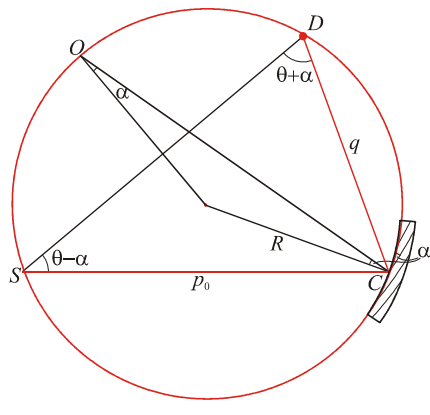
Figure 3. The scattering geometry in asymmetric case. A Johansson (i.e. ground-bent) crystal is shown, the surface of which lies on the Rowland circle and the Bragg planes have the doubled curvature radius (i.e. with the curvature center in O).

$d_{SD}=2R\sin2\theta$, (i.e. independent of α)
$p_0=2R\sin(\theta+\alpha)$,
$q=2R\sin(\theta-\alpha)$,
Sagittal crystal radius:
$R_{sag}=2\sin\theta\cdot pq/(p+q)$
$R_{sag}(p=p_0)=R(\cos2\alpha-\cos2\theta)$
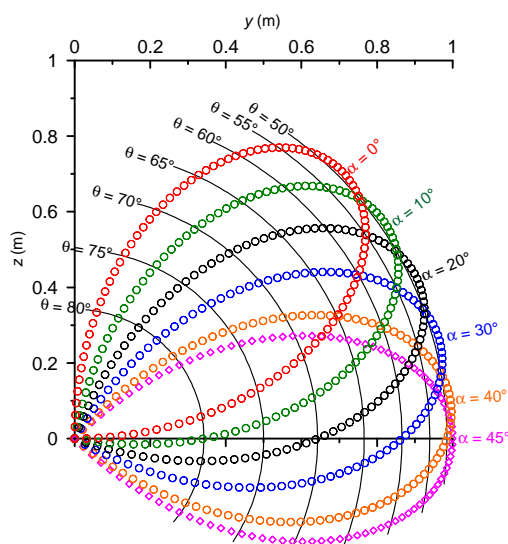
Figure 4. The detector position at different asymmetry and Bragg angles. The crystal here is always on the $0y$ axis positioned at the distance $p_0(\theta,\alpha)$.
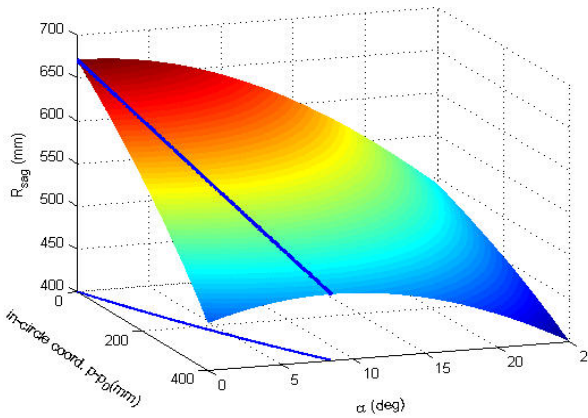
Figure 5. The sagittal bending radius of the analyzer crystal. The blue line shows the position of the maximum at certain in-circle coordinate $p_0–p$.

Table 6. Images at different asymmetry angles. The relative flux is given above each image for an energy-uniform isotropic source (transmittivity $T = (I/N_{rays})\cdot(\Delta E_{geom.source}/\Delta E)\cdot(\Omega_{geom.source}/\Omega)$, flux $\Phi \propto T\cdot \Omega\cdot\Delta E$).

	α=0°	5°	10°	15°	20°	25°
on circle (p=p_0)	≡100%	90%	80%	73%	65%	59%
in circle ($p_0–p$=400 mm)	≡100%	79%	67%	56%	51%	42%

Observations:

Advantages of asymmetry:

1. Smaller image size. Thus the 1D detector for energy dispersive in-circle images can be significantly smaller.

2. The sagittal bending radius has a maximum at α>0 when in in-Rowland circle condition (see Figure 5). However, this maximum is weak: only +10% from $R_{sag}(\alpha$=0) at large in-circle coordinate $p_0–p$=400 mm.

3. The sample-detector distance is independent of α. However, its projection to the beamline axis is longer at α>0 thus allowing for bigger sample environments.

Disadvantages of asymmetry:

1. Smaller flux because the crystal is situated further away from the source at larger α.

2. Non-uniform flux distribution. However, for the in-circle images the integrated vertical (energy dispersive) distribution is uniform.

Summary:

The effects of asymmetry are only visible at large asymmetry angles, where flux is lowering and the sagittal radius is small. The advantage of maximizing the sagittal radius at *small* asymmetry angles is too small. Thus, the asymmetry is not recommended.

8   Johansson-like diced crystal (symmetric and asymmetric)

A Johansson crystal is a ground-bent crystal where the crystal surface lies on the Rowland circle while the Bragg planes have the doubled curvature radius. In the diced form the crystal facets are not bent, so that to obtain a Johansson-like geometry, the facets must have the asymmetry angle variable in the diffraction plane. For R=50 cm and the crystal length 10 cm the asymmetry angle should vary in the range $\alpha \approx \alpha_0 \pm 3°$.

Note on ray tracing: A Johansson geometry requires the meridional radius (R=50 cm) to be smaller than the sagittal radius for short (and zero) in-circle coordinates (see Figure 5). Unfortunately, the Shadow code fails to generate such a toroidal surface in combination with the faceted case. Therefore below only a deep-in-circle Johansson-like case is considered, where $R_{sag}<R$.

Table 7. Images for Johansson-like diced crystal at different central asymmetry angles.
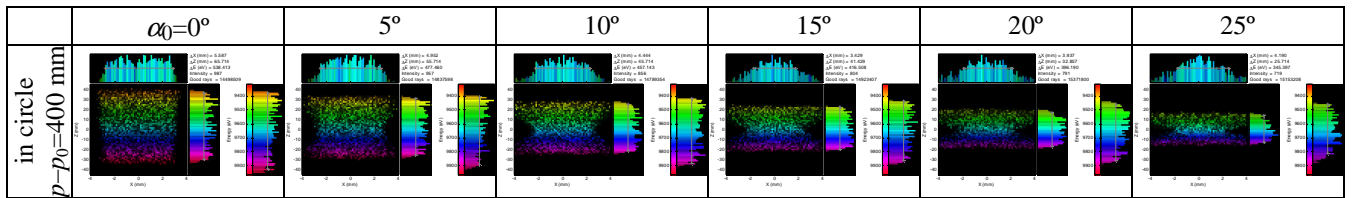
Observations:

The flux here is the same (within statistical errors) in comparison to the case of constant asymmetry angles (see Table 6).

Summary:

A Johansson-like diced crystal gives no intensity gain in comparison with a simple diced crystal (Johann-like) of the same facet size. However, energy resolution in these two cases is essentially different (see Section 9.3).

9   Energy resolution

9.1   Influence of elastic deformations

Bending a crystal results in elastic deformations that affect energy resolution [9]: $\Delta E/E = t/R \cdot |\cot^2\theta - \sigma|$, where t is the crystal thickness and σ is the Poisson ratio of the crystal material.
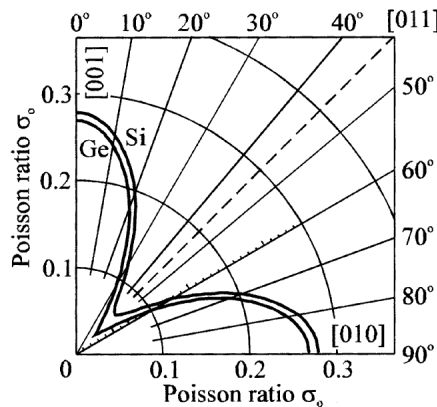
Figure 6. Si, Ge. Poisson ratio vs. direction in the (001) plane. Taken from [10].

Aiming at the energy resolution better than the natural width of $K\alpha$ lines, $\Delta E/E \approx 2 \cdot 10^{-4}$, the required thickness can be estimated as 0.3–0.4 mm for the usable range of Bragg angles. **The necessity of thin crystals for good energy resolution is another argument (in addition to energy dispersion) in favor of the diced crystal shape with flat facets.**

Notice that the energy distributions obtained above from ray tracing do not take into account any elastic deformations. Thus the estimations given for the non-diced crystals are too optimistic.

9.2   Energy resolution of simple diced crystal (Johann-like)

Energy resolution was estimated in the following way. Consider the fluorescence spectrum consisting of a single sharp line. It results in an image of a finite width in the diffraction plane. Two fluorescence lines are resolved if their images are separated by dz that is wider than the width of a single line. The energy separation between these two lines is assumed to follow dE/dz = $\Delta E/\Delta z$, where ΔE is the energy acceptance of the crystal and Δz is the image width of an energy-uniform source. Thus the energy resolution is given by:

dE = FWHM(single line)·$\Delta E/\Delta z$

Table 8. To the determination of energy resolution. The upper images are for a uniform source, the lower ones are for a single line source.
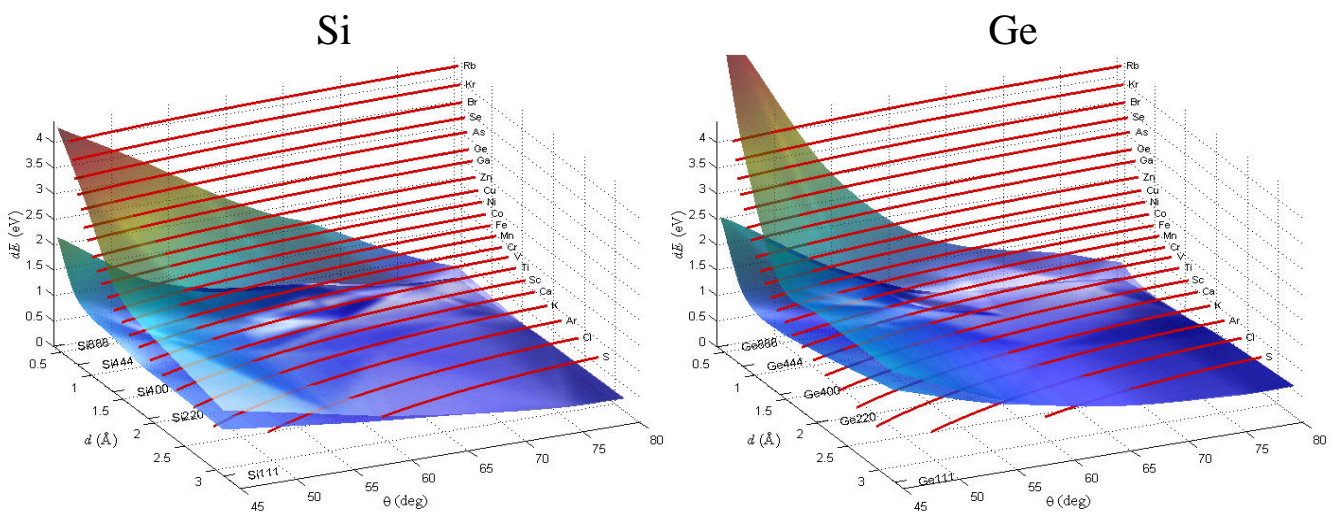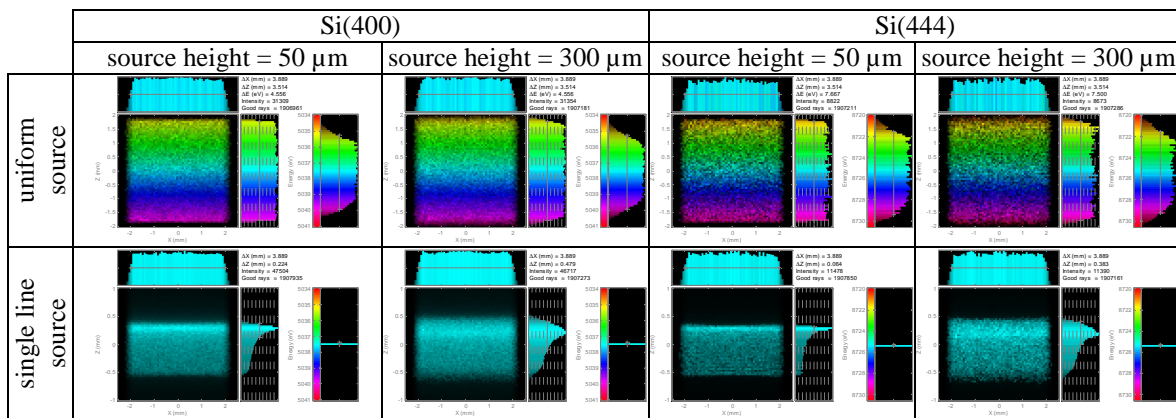
Figure 7. Ray-traced energy resolution. Upper (lower) sheets are for 300(50)-µm-high beam spot at the sample. The horizontal red lines are $K\alpha$ natural widths [11] in d-θ planes.

Observations:

At small Bragg angles the energy resolutions for a 50-µm and a 300-µm beam differ significantly. Even for the 300-µm beam (which is a very conservative estimation for the

beam height), energy resolution at $\theta{>}55°$ for Si crystals is always better than the $K\alpha$ widths.

The energy resolution for Si(400) and Ge(400) are nearly equal. Taking into account a more than two times gain in intensity for Ge, the Ge(400) crystal should be selected.

Table 9. Ray-traced energy resolution at the highest possible Bragg angles.

element		$K\alpha$ width (eV) [11]	Si				Ge			
			crystal	$\theta_{K\alpha}$ (°)	dE (eV) at 50µm	dE (eV) at 300µm	crystal	$\theta_{K\alpha}$ (°)	dE (eV) at 50µm	dE (eV) at 300µm
16	S	0.59	111	58.95	0.56	0.66	111	55.32	1.12	1.17
17	Cl	0.64		48.93	0.78	1.07		46.36	1.72	2.01
18	Ar	0.68		41.95	0.99	1.43		39.92	2.11	2.61
19	K	0.74	220	76.99	0.20	0.23	220	69.27	0.56	0.60
20	Ca	0.81		61.00	0.39	0.69		57.09	0.99	1.16
21	Sc	0.86		52.12	0.58	1.10		49.26	1.26	1.76
22	Ti	0.94		45.71	0.89	1.62	400	76.34	0.29	0.35
23	V	1.01	400	67.22	0.27	0.54		62.26	0.59	0.90
24	Cr	1.08		57.48	0.33	0.89		54.05	0.77	1.43
25	Mn	1.16		50.72	0.66	1.52	333	74.85	0.23	0.41
26	Fe	1.25	333	67.86	0.12	0.47	440	75.45	0.21	0.40
27	Co	1.33	440	68.71	0.11	0.49		63.43	0.33	0.92
28	Ni	1.44		59.71	0.24	1.09		55.99	0.50	1.29
29	Cu	1.55	444	79.31	0.10	0.28	444	70.61	0.20	0.66
30	Zn	1.67		66.27	0.12	0.73		61.49	0.35	1.11
31	Ga	1.82		58.73	0.30	1.52		55.14	0.56	1.58
32	Ge	1.96	660	78.45	0.11	0.34	555	73.70	0.20	0.64
33	As	2.14	555	69.65	0.13	0.76		64.15	0.34	1.20
34	Se	2.33		61.75	0.32	1.51		57.73	0.66	1.79
35	Br	2.52		56.00	0.56	2.34		52.73	0.99	2.69
36	Kr	2.75		51.40	0.90	3.05	880	78.58	0.12	0.46
37	Rb	2.99	880	74.61	0.13	0.70		67.76	0.30	1.08
38	Sr	3.25	777	77.71	0.11	0.49	777	69.71	0.28	1.00
39	Y	3.52		67.71	0.38	1.47		62.65	0.51	1.60
40	Zr	3.82		61.33	0.61	2.23	10,10,0	79.25	0.11	0.48
41	Nb	4.14	10,10,0	76.32	0.13	0.70		68.87	0.30	1.12
42	Mo	4.52		67.46	0.46	1.69		62.46	0.56	1.72
43	Tc	4.91		61.52	0.70	2.42		57.54	1.06	2.66
44	Ru	5.33		56.86	0.89	3.04		53.50	1.47	3.59
45	Rh	5.77		52.99	1.20	3.50		50.05	1.94	4.77
46	Pd	6.24		49.67	1.66	3.91		47.04	2.42	5.95
47	Ag	6.75		46.75	2.13	4.27		44.37	2.81	6.92
48	Cd	7.28		44.16	2.52	4.59		41.97	3.16	7.78
49	In	7.91		41.82	2.86	4.87		39.80	3.49	8.57

9.3　Energy resolution of Johansson-like diced crystal

As mentioned in Section 8, the Shadow code cannot generate a faceted toroidal surface with the meridional radius smaller than the sagittal radius (this functionality was left not implemented). Therefore a complete study of the Johansson-like diced case is impossible; this *is* possible at Bragg angles ≤ 45°. At θ=45°: $R_{mer}= R_{sag} =R$ (Rowland circle radius). The energy resolution was calculated in the same way as in Section 9.2 and additionally proved with a 7-lines source.

Table 10. To the determination of energy resolution. Comparison of the Johansson-like case with a simple diced case (Johann-like) for Si(444) at $\theta=45°$ and a 50 µm source height.

	Johann-like	Johansson-like
uniform source	ΔX (mm) = 4.000, ΔZ (mm) = 2.750, ΔE (eV) = 21.875, Intensity = 23307.93, Good rays = 14847504	ΔX (mm) = 4.000, ΔZ (mm) = 5.625, ΔE (eV) = 44.531, Intensity = 23238.57, Good rays = 14811454
single line source	ΔX (mm) = 4.000, ΔZ (mm) = 0.213, ΔE (eV) = 0.002, Intensity = 49891.46, Good rays = 14847730	ΔX (mm) = 4.000, ΔZ (mm) = 0.070, ΔE (eV) = 0.002, Intensity = 26215.33, Good rays = 14809769
dE	1.69 eV	0.55 eV
7 lines source with $\Delta E_{\text{inter-line}} = \text{d}E$	ΔX (mm) = 3.950, ΔZ (mm) = 1.493, ΔE (eV) = 10.206, Intensity = 46728.20, Good rays = 14847522	ΔX (mm) = 4.000, ΔZ (mm) = 0.477, ΔE (eV) = 3.349, Intensity = 26254.81, Good rays = 14809479

cf. Darwin width = 0.067 eV
$\Delta E_{\text{Se }K\alpha1}$ (E=11222) = 3.33 eV

Observations:

For the 10 considered crystals, the Johansson-like case gives 2.5-3 times better energy resolution than the Johann-like case. This difference is much more pronounced if based not on FWHM of a line image but rather on the full width or the width at a lower level, e.g. 10%.

The proposed way of determination of energy resolution gives the spatial separation between different fluorescence lines similar to that given by the Rayleigh criterion.

The Johansson-like crystal has larger energy acceptance. The flat top in the energy distribution is ~3 times larger. Therefore the dice size can be decreased down to ~1 mm. In this way the Johansson-like crystal has about the same flat top in the energy distribution as the Johann-like crystal has, but has 2.5-3 times better energy resolution and an increased by ~150% crystal efficiency.

10   Expected flux at detector

The flux at the detector is given by

$$\Phi_f = \Phi_{inc}\, \frac{\mu_A(E)}{\mu_T(E)+\mu_T(E_f)}\, \varepsilon_f\, \frac{\Omega}{4\pi}\, \frac{\min(\Delta E, \Delta E_{K\alpha})}{\Delta E_{K\alpha}}\, T \;,$$

where ε_f is the fluorescence yield, Ω is the solid angle accepted by the crystal; μ is absorption coefficient: atomic (A) and total (T) at an energy above the edge and at the energy of the fluorescence line; T is the transmittivity of the crystal obtained from ray tracing as $T = (I/N_{rays})\cdot(\Delta E_{geom.source}/\Delta E)\cdot(\Omega_{geom.source}/\Omega)$; the factor $\min(\Delta E,\ \Delta E_{K\alpha})/\Delta E_{K\alpha}$ determines whether the fluorescence line goes through the energy acceptance window ΔE of the analyzer, at present conditions =1; the ratio $\mu_A(E)/[\mu_T(E)+\mu_T(E_f)]$ is just below unity for pure materials, is typically 0.05 for catalytic samples (~1 wt% of a metal in a light matrix) and can be 10^{-5} for an 'environmental' sample (1 ppm of a quite heavy element in a relatively light matrix). The incidence flux Φ_{inc} was estimated in Ref. [1]. $\Omega(55°)=0.01$ sr.

Table 11. Expected flux at the detector for three samples of different concentrations. $\theta = 55°$.

crystal		Φ_{inc} (ph/s)	element	$\varepsilon_f(K\alpha)$	Φ_f (ph/s)		
					pure	'1 wt %'	'1 ppm'
111	Si	$1\cdot10^{13}$	S	0.07	$1\cdot10^7$	$8\cdot10^5$	150
	Ge				$3\cdot10^7$	$2\cdot10^6$	320
220	Si	$1\cdot10^{13}$	Sc	0.17	$2\cdot10^7$	$1\cdot10^6$	270
	Ge				$6\cdot10^7$	$3\cdot10^6$	650
400	Si	$1\cdot10^{13}$	Cr	0.27	$2\cdot10^7$	$1\cdot10^6$	210
	Ge				$4\cdot10^7$	$3\cdot10^6$	500
444	Si	$1\cdot10^{13}$	Ge	0.5	$8\cdot10^6$	$5\cdot10^5$	90
	Ge				$2\cdot10^7$	$1\cdot10^6$	200
888	Si	$1\cdot10^{12}$	Ru	0.8	$1\cdot10^5$	$8\cdot10^3$	2
	Ge				$3\cdot10^5$	$2\cdot10^4$	3

11   Crystal thickness
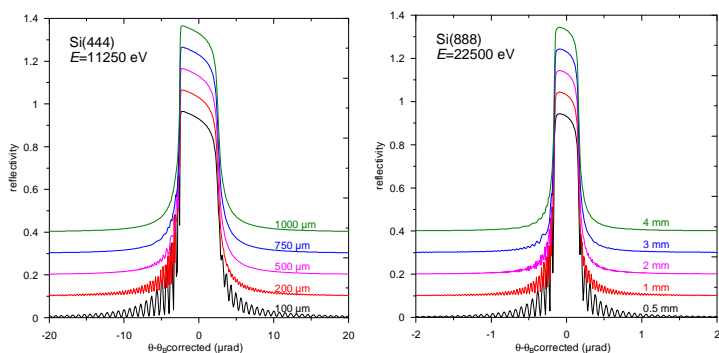
Figure 8. Diffraction curves of high orders (s-polarization) for crystals of different thickness.

Summary:

The fringes in the diffraction curves are absent for thick crystals. For the highest orders considered in this CDR, the thickness should be > ~2–3 mm. This issue is to be discussed with the manufacturer of the crystals.

12 Notes on influence of Compton and Rayleigh scattering

The traditional positioning of a fluorescence detector or a fluorescence analyzer at 90º to the photon beam in the polarization plane has the advantage that the coherent scattering is minimized. In this case its cross section goes to zero for horizontally polarized photons. However, the elastic line is required for energy calibration and will be extensively used in the presented spectrometer.

For light elements, Compton scattering can be more intense than Rayleigh scattering in the energy range of interest (2–30 keV). The Compton peak is rather wide because of multiple Compton scattering and scattering off valence electrons. The Compton wavelength shift $\Delta\lambda=\lambda_c(1-\cos\theta)$ is zero for the forward scattering and maximal for the back scattering. It appears that the scattered photons which initially had energy near a K-absorption edge have final energy near and below the corresponding $K\beta$ line energy (but still quite above the $K\alpha$ line energy) for scattering at 90º. Back scattering (180º) leads to a larger shift, away from the $K\beta$ line, thus enabling a more precise $K\beta$ spectroscopy.

Summary:

The spectrometer should have provisions to be installed before the sample, at 90º and behind the sample to enable the study of influence of Compton and Rayleigh scattering.

13 Detectors

S. Huotari et al. [8] reported the usage of a Medipix2 photon-counting pixel detector (14×14 mm^2, 256×256 pixels) for a diced crystal of 0.7×0.7 mm^2 facets. In our case this detector would be even more efficient because its size matches better to the image size ($\sim4\times4$ mm^2).

For wide energy dispersive images in in-circle geometry the Mythen detector [12] seems to be appropriate: 1280 strips with a length (x) of 8 mm and a pitch (z) of 50 µm, the total detector length (z) is 64 mm.

It is foreseen that non-spatial resolving detectors (e.g. Hamamatsu APD) are also used for applications which need a larger dynamic range.

14 Vacuum tank
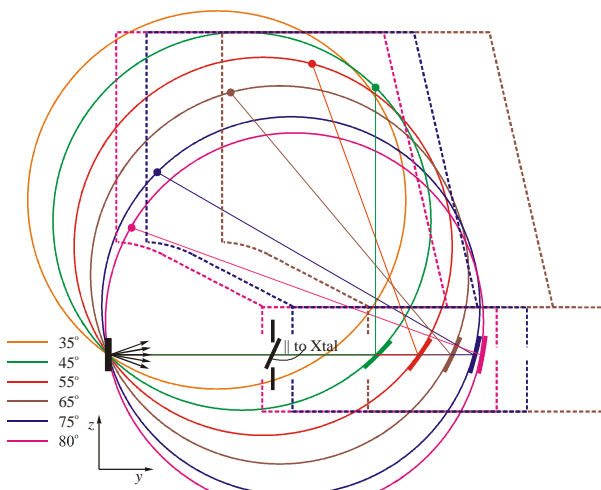
Figure 9. The spectrometer with vacuum tank, crystal analyzer and detector positioned at different Bragg angles. The Rowland circle diameter = 1m.

The spectrometer should be rotatable around the sample-crystal axis to switch between vertical and horizontal configurations.

In vertical configuration, the blue position of the tank allows for insertion of a Ø200 mm vertical device (cryostat); the brown position of the tank allows for insertion of a Ø600 mm vertical device (magnet). Correspondingly changes the maximal allowed Bragg angle.

In horizontal configuration, there is always space for a Ø600 mm vertical device with unconstrained Bragg angle.

15 Further considerations

To reduce the scattering and fluorescence from the vacuum tank walls, the spectrometer should have a slit system before the crystal analyzer. The blades moving perpendicular to the diffraction plane should be adjustable in parallel to the crystal in order to exactly match the slit opening with the crystal size.

The two windows of the spectrometer (presumably of Kapton) should be easily removable in order to integrate the spectrometer into the sample volume and the beamline vacuum system.

In the position of the spectrometer behind the sample it can be used as a reflectometer in order to be able to discriminate the elastically scattered beam from fluorescence.

In the position of the spectrometer facing not to the sample but to the monochromatic beam it can be used as a polarimeter in order to facilitate the setup of the quarter-wave plates (QWP). The detailed study on the QWP is available on the beamline web page.

16 Summary of the design proposal

- The x-rays are back scattered from the sample in order to collect fluorescence through the input window of an in-situ cell or a cryostat. Thus no additional side window is required.

- The geometry allows for energy dispersive images in two scales: some eV (due to diced crystal) and some hundreds eV (due to in-Rowland circle position of the sample). Thus no θ–2θ scans are required.

- 3 diced crystals: Si(111), Si(220) and Ge(400) splitted into two halves with $(2\ mm)^2$ or $(1\ mm)^2$ facets in a simple Johann-like or Johansson-like cases, respectively. The Johansson-like case is preferred for its better energy resolution. One additional Ge crystal, (111) or (220), for high order diffraction is desirable due to its higher (relatively to Si) reflectivity. The crystals cover the energies 2–~22 keV with energy resolution better than the width of the corresponding $K\alpha$ lines.

- Dynamical sagittal crystal bending, which depends on Bragg angle and in-circle coordinate, allows for small sagittal image size. Thus 1D, not 2D, detectors are required.

- The movable tank allows for insertion of large sample infrastructures and also enables completely windowless operation.

17 3D models of the spectrometer

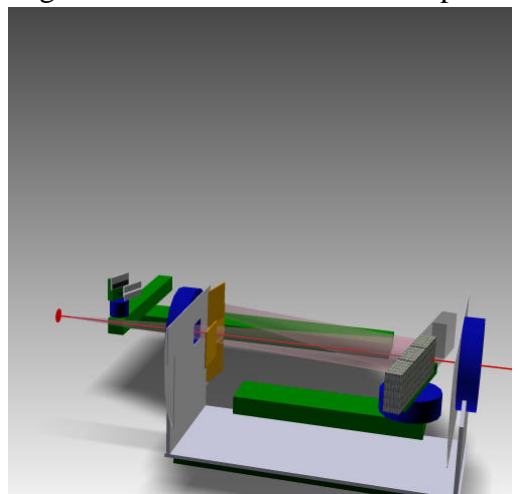Figure 10. Vertical diffraction plane.   Figure 11. Horizontal diffraction plane.
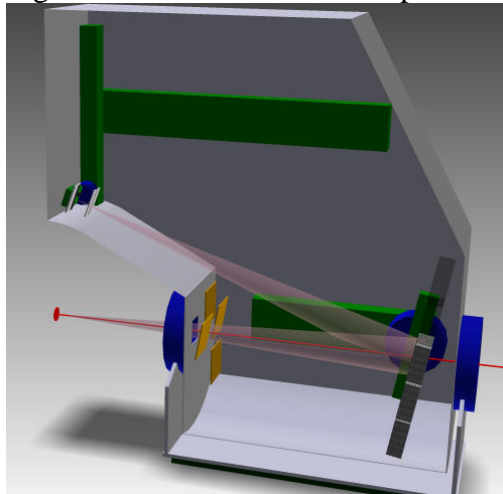
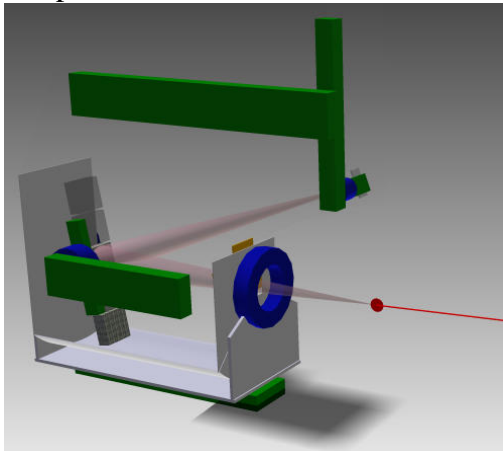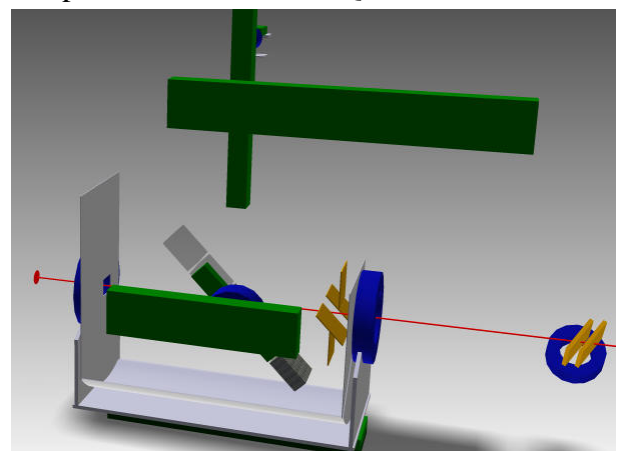Figure 12. Positioning behind the sample for ReflXAFS

Figure 13. Usage of the spectrometer as polarimeter with two QWPs.

The 3D figures can be viewed animated at the beamline web page:
http://www.cells.es/Beamlines/XAS/ .

18   Technology for the Diced crystals

1) Grinding a meridional cylinder with R=1000 and total sagittal length of 150.

2a) Incomplete cuts in sagittal direction (perp. to the sketch) leaving a ~100 µm membrane. *Option: a glued glass membrane as in* [13] *with complete crystal cuts down to the glass*.

Notice that the cuts all stop at an equal distance to the flat support. This makes the dicing easier using a disk dicing machine and results in a uniform membrane thickness.

2b) Complete meridional cuts (parallel to the sketch) resulting in separate crystal columns.

3) Putting on a reference R=500 cylinder.

4) Clamping to the reference cylinder.

5) Gluing Al support columns which have one surface machined to R=1000. The distance from the bending support to the reference cylinder is assured to be constant. Notice that the accuracy of the support columns is not critical and alleviated by the glue layer.

6) Thermal pre-treatment in order to prepare a hydrophilic surface. Chemical etching of the optical surface. Turn up, insert the bending support stripes.
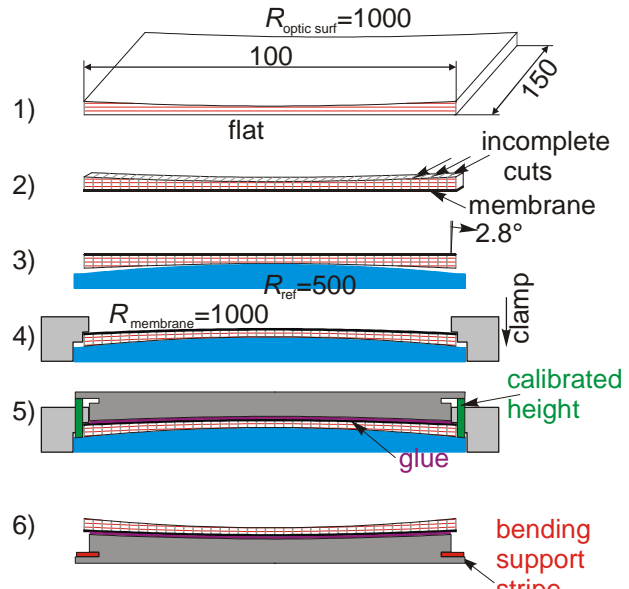
An example of a spherically bent diced analyzer crystal can be found in [13]. They used a low-viscosity epoxy glue Epotek 301-2 and a Kulicke and Soffa 984-10 Plus dicing machine. The cutting speed was 1 mm/s at a spindle speed of 20000 r.p.m. The width of the cuts was 100 µm and the pixel size was 450 µm × 850 µm.

References

[1] K. Klementiev, *Conceptual Design Report "XAS beamline at the ALBA Synchrotron Light Facility"* (2006) (see web page: http://www.cells.es/Beamlines/XAS/).

[2] M. Lemonnier, R. Fourme, F Rousseaux, and R. Kahn. *X-ray curved crystal monochromator system at the storage ring DCI*. Nuclear Instruments and Methods*.,* **152** (1978) 173–177.

[3] T. Matsushita and U. Kaminaga, *A Systematic Method of Estimating the Performance of X-ray Optical Systems for Synchrotron Radiation. II. Treatment in Position-Angle-Wavelength Space*, J. Appl. Cryst. **13** (1980) 472–478.

[4] E. Welter, P. Machek, G. Dräger, U. Brüggmann and M. Fröba, *A new X-ray spectrometer with large focusing crystal analyzer*, *J. Synchrotron Rad.* **12** (2005) 448–454.

[5] K. Klementiev, *Energy-dispersive Shadowrunner* (2007) based on Matlab script *Shadowrunner* by J. Juanhuix and J. Nicolás (2005).

[6] B. Lai and F. Cerrina, Nuc. Instrum. Methods A **246** (1986) 337.

[7] M. Sanchez del Rio, R. J. Dejus, *XOP: A Multiplatform Graphical User Interface for Synchrotron Radiation Spectral and Optics Calculations,* SPIE Proc., 3152 (1997) 148; web page: http://www.esrf.fr/computing/scientific/xop2.1/.

[8] S. Huotari, Gy. Vankó, F. Albergamo, C. Ponchut, H. Graafsma, C. Henriquet, R. Verbeni and G. Monaco, *Improving the performance of high-resolution X-ray spectrometers with position-sensitive pixel detectors*, J. Synchrotron Rad. **12** (2005) 467–472.

[9] P. Suortti and A. K. Freund, *On the phase-space description of synchrotron x-ray beams*, Rev. Sci. Instrum. **60** (1989) 2579–2585.

[10] J.J. Wortman and R.A. Evans, *J. Appl. Phys.* **36** (1965) 153.

[11] M. O. Krause and J. H. Oliver, *Natural widths of atomic K and L levels, Kα X-ray lines and several KLL Auger lines*, J. Phys. Chem. Ref. Data **8** (1979) 329–338.

[12] B. Schmitt, Ch. Brönnimann, E.F. Eikenberry, F. Gozzo, C. Hörmann, R. Horisberger, B. Patterson, *Mythen detector system*, Nucl. Instr. and Meth. A **501** (2003) 267–272.

[13] J. P. Hill, D. S. Coburn, Y.-J. Kim, T. Gog, D. M. Casa, C. N. Kodituwakku and H. Sinn, *A 2 m inelastic X-ray scattering spectrometer at CMC-XOR, Advanced Photon Source*, J. Synchrotron Rad. **14** (2007) 361.